

Mapping growth windows in quaternary perovskite oxide systems by hybrid molecular beam epitaxy

Matthew Brahlek, Lei Zhang, Hai-Tian Zhang, Jason Lapano, Liv R. Dedon, Lane W. Martin, and Roman Engel-Herbert

Citation: *Applied Physics Letters* **109**, 101903 (2016); doi: 10.1063/1.4962388

View online: <http://dx.doi.org/10.1063/1.4962388>

View Table of Contents: <http://scitation.aip.org/content/aip/journal/apl/109/10?ver=pdfcov>

Published by the [AIP Publishing](#)

Articles you may be interested in

[Avoiding polar catastrophe in the growth of polarly orientated nickel perovskite thin films by reactive oxide molecular beam epitaxy](#)

AIP Advances **6**, 085115 (2016); 10.1063/1.4961700

[Growth of SrVO₃ thin films by hybrid molecular beam epitaxy](#)

J. Vac. Sci. Technol. A **33**, 061504 (2015); 10.1116/1.4927439

[Self-regulated growth of LaVO₃ thin films by hybrid molecular beam epitaxy](#)

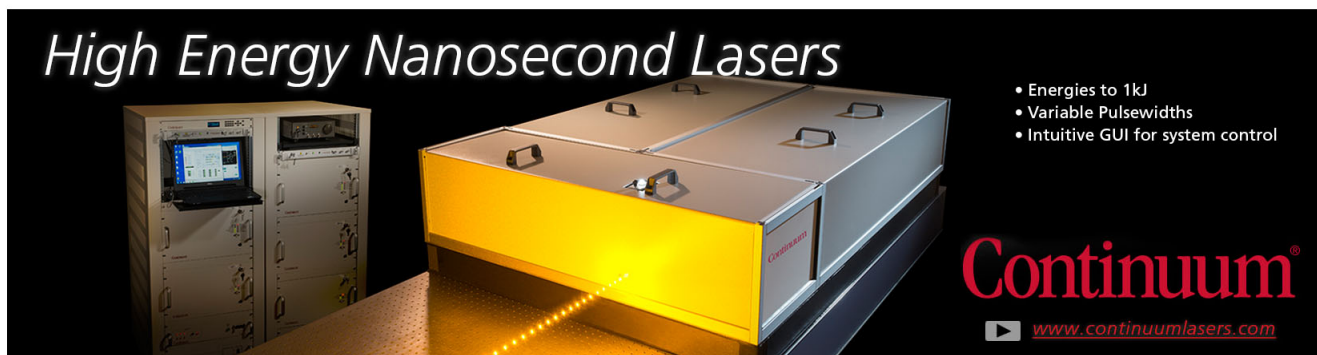
Appl. Phys. Lett. **106**, 233102 (2015); 10.1063/1.4922213

[Surface reconstructions in molecular beam epitaxy of SrTiO₃](#)

Appl. Phys. Lett. **105**, 191901 (2014); 10.1063/1.4901726

[Growth of high-quality SrTiO₃ films using a hybrid molecular beam epitaxy approach](#)

J. Vac. Sci. Technol. A **27**, 461 (2009); 10.1116/1.3106610

The advertisement features a black background with the text 'High Energy Nanosecond Lasers' in a white, italicized serif font at the top left. Below the text, there is a photograph of a laser system consisting of a control rack on the left and a large, rectangular laser head on the right. The laser head is illuminated from below, casting a bright yellow glow. A red laser beam is visible, extending from the front of the laser head towards the bottom left. On the right side of the advertisement, there is a list of features: 'Energies to 1kJ', 'Variable Pulsewidths', and 'Intuitive GUI for system control'. At the bottom right, the 'Continuum' logo is displayed in a red, serif font, with a registered trademark symbol. Below the logo is a small YouTube icon followed by the website address 'www.continuumlasers.com' in a red, sans-serif font.

Mapping growth windows in quaternary perovskite oxide systems by hybrid molecular beam epitaxy

Matthew Brahlek,¹ Lei Zhang,¹ Hai-Tian Zhang,¹ Jason Lapano,¹ Liv R. Dedon,^{2,3} Lane W. Martin,^{2,3} and Roman Engel-Herbert^{1,a)}

¹Department of Materials Science and Engineering, Pennsylvania State University, University Park, Pennsylvania 16801, USA

²Department of Materials Science and Engineering, University of California, Berkeley, California 94720, USA

³Materials Science Division, Lawrence Berkeley National Laboratory, Berkeley, California 94720, USA

(Received 21 June 2016; accepted 23 August 2016; published online 7 September 2016)

Requisite to growing stoichiometric perovskite thin films of the solid-solution $A'_{1-x}A_xBO_3$ by hybrid molecular beam epitaxy is understanding how the growth conditions interpolate between the end members $A'BO_3$ and ABO_3 , which can be grown in a self-regulated fashion, but under different conditions. Using the example of $La_{1-x}Sr_xVO_3$, the two-dimensional growth parameter space that is spanned by the flux of the metal-organic precursor vanadium oxytriisopropoxide and composition, x , was mapped out. The evolution of the adsorption-controlled growth window was obtained using a combination of X-ray diffraction, atomic force microscopy, reflection high-energy electron-diffraction (RHEED), and Rutherford backscattering spectroscopy. It is found that the stoichiometric growth conditions can be mapped out quickly with a single calibration sample using RHEED. Once stoichiometric conditions have been identified, the out-of-plane lattice parameter can be utilized to precisely determine the composition x . This strategy enables the identification of growth conditions that allow the deposition of stoichiometric perovskite oxide films with random A-site cation mixing, which is relevant to a large number of perovskite materials with interesting properties, e.g., high-temperature superconductivity and colossal magnetoresistance, that emerge in solid solution $A'_{1-x}A_xBO_3$. Published by AIP Publishing. [<http://dx.doi.org/10.1063/1.4962388>]

Electronic phases that emerge by chemically interpolating between two compounds with dissimilar ground states represent some of the most fascinating and widely studied areas of condensed matter physics and materials science. This ranges from metal-to-insulator (MIT) transitions,¹ emergence of high-temperature superconductivity,² topological phase transitions,^{3–5} novel coupled MIT-magnetic phases,⁶ optimization of band gaps, band offsets, and lattice parameters in semiconductors,⁷ and optimization of piezoelectricity and ferroelectricity.⁸ This is particularly true for the transition metal oxides (TMO) class of materials where high-temperature (high- T_C) superconductivity emerges at the boundary between a Mott insulator and Fermi liquid, like the first discovered high- T_C material $La_{1-x}Ba_xCuO_4$,⁹ and the colossal magneto-resistance effect found in compounds like $La_{1-x}Sr_xMnO_3$.^{10–12} Further, alloying is used to position materials close to a morphotropic phase boundaries to maximize ferroelectric and piezoelectric responses, e.g., $Pb(Zr_{1-x}Ti_x)O_3$, a key material in capacitors, piezoelectric actuators, and transducers.⁸

Of interest here is the Mott transition between the d^2 Mott insulator $LaVO_3$ and the strongly correlated d^1 metal $SrVO_3$.^{13,14} For the A-site cation mixed compound $La_{1-x}Sr_xVO_3$ tuning, the La-to-Sr ratio (herein referred to as *composition*, rather than *stoichiometry* which will be reserved to refer to the (La + Sr)-to-vanadium ratio) effectively changes the band filling, which, in turn, drives an insulator-to-metal transition that is accompanied by an

antiferromagnetic-to-paramagnetic order transition and melting of an orbitally ordered state.¹⁵ The key to harness and understand many of the complex and intertwined properties of TMOs in general, and $La_{1-x}Sr_xVO_3$ in particular, is to precisely control the synthesis of the materials to avoid confounding intrinsic properties with extrinsic disorder related effects that can, for example, the ABO_3 perovskite-based materials, stem from deviations from the ideal A-to-B cation ratio. Such extrinsic defects can compete with intrinsic effects related to electron-electron correlations.¹⁶

In thin films, the growth of solid-solution oxide compounds is challenging since the composition is difficult to control. Techniques like sputtering and pulsed-laser deposition (PLD), both of which utilize stoichiometric targets, can transfer material to the film in the correct ratio, but, when materials are composed of elements with different volatilities, the high incident energies used can preferentially eject the more volatile element resulting in non-stoichiometric films.¹⁷ Further, since these techniques rely on premixed targets, each composition requires a separate target, which makes compositional studies difficult. In contrast, solid source molecular beam epitaxy (MBE) makes use of thermal evaporation of source material, which is orders-of-magnitude lower in incident energy than sputtering and PLD, and simultaneously gives the ability to directly control the composition to within $\sim 1\%$ accuracy. This limited accuracy, however, generates an additional challenge for MBE, which, for the case of the perovskites, limits the accuracy of the stoichiometry. Extending MBE to include metal-organic (MO) sources for the B-site ion—called hybrid MBE (hMBE)—alleviates

^{a)}Author to whom correspondence should be addressed. Electronic mail: rue2@psu.edu

this difficulty for certain materials because an adsorption-controlled growth regime, called a growth window, is opened.¹⁸ The ever-expanding list of materials successfully synthesized by hMBE now includes SrTiO₃,¹⁹ BaTiO₃,²⁰ GdTlO₃,²¹ NdTiO₃,²² SrVO₃,²³ LaVO₃,²⁴ and BaSnO₃²⁵ and has proven to produce the highest-quality perovskite films with the highest mobility in SrTiO₃,^{26,27} resulting in the observation of quantum Hall effect,²⁸ and the highest residual resistance ratio in SrVO₃.²⁹

Unlike binary semiconductors, which also grow in an adsorption controlled manner,³⁰ the growth window for hMBE perovskites is relatively narrow, and thus, careful flux control is required. Further, determining the optimal conditions requires the growth of many samples, each at a different pressure of the MO gas source, which are then used to determine a minimum in lattice parameter. This time consuming and tedious calibration method commonly applied to ternary perovskite oxides is not practical for studying or optimizing simultaneously with respect to multiple deposition variables, as in the case of quaternary material systems. Although Ba_{1-x}Sr_xTiO₃ has been grown for $x = 0.19, 0.35, \text{ and } 0.46$ by hMBE,³¹ a systematic study on the optimization of the growth window with composition x is lacking. Here, we combine solid source thermal effusion cells for La and Sr with vanadium oxytriisopropoxide (VTIP) for the vanadium source to grow La_{1-x}Sr_xVO₃ thin film by hMBE in the entire composition range $x = 0-1$ on (001) (La_{0.3}Sr_{0.7})(Al_{0.65}Ta_{0.35})O₃ (LSAT) substrates. Using a combination of X-ray diffraction (XRD), atomic force microscopy (AFM), reflection high-energy electron diffraction (RHEED), and Rutherford backscattering spectrometry (RBS), we show how the growth window evolves as a function of dosed VTIP for different compositions x of La_{1-x}Sr_xVO₃. Further, in contrast to previous growth window studies that required many samples,^{23,24} we find that the optimal growth conditions can also be determined quickly and reliably using a single calibration sample and RHEED. This strategy paves the way towards a better understanding of the growth window in hMBE by allowing exploration of a larger growth parameter space that includes commonly fixed growth parameters, such as growth temperature and growth rate.

Films were grown using a DCA M600 hMBE equipped with thermal effusion cells for Sr and La, and gas injectors for molecular oxygen and a metal-organic source for 99.99% VTIP, which was supplied by maintaining a constant gas inlet pressure, P_{VTIP} , on the upstream side of the gas injector (see Ref. 23 for more details); P_{VTIP} will be used to reference the growth conditions of the samples. Prior to growth, La and Sr were calibrated *in situ* by a quartz crystal microbalance (QCM) to target a total (La + Sr) flux of $\sim 2.50 \times 10^{13} \text{ cm}^{-2} \text{ s}^{-1}$. A-site composition x and thickness were measured *ex situ* by RBS and XRD; any deviation from the targeted A-site flux was accounted for by multiplying P_{VTIP} by targeted flux over the experimental flux. LSAT substrates were cleaned *in situ* prior to the growth by heating them up to a substrate temperature of 900 °C, as measured by the thermocouple mounted between the substrate heater and substrate, and exposing them for ~ 10 min to an oxygen plasma supplied by a radio-frequency plasma source operated at 250 W.

After cleaning, all the films were deposited at a substrate temperature of 900 °C, in molecular oxygen with a background pressure of $\sim 5 \times 10^{-7}$ Torr, and using a constant deposition time that yielded a thickness of ~ 26 nm (except the SrVO₃ sample, which was 50 nm).

Previously it has been shown that the growth windows exist for both LaVO₃ and SrVO₃.^{23,24} The primary means to identify this was to track the c -axis lattice parameter versus P_{VTIP} . Inside the growth window, the lattice parameter for SrVO₃ is constant and a minimum.²³ This can be explained by the perovskite lattice which hosts non-stoichiometric defects by creating vacancies on the other cation site.³² For example, excess Sr and V are accommodated by the formation of SrO stacking faults (i.e., Sr_{1+ δ} VO₃) and phase precipitation of rocksalt VO_x in the SrVO₃ film matrix;³³ both of which cause expansion of the out-of-plane film lattice parameter. In contrast, defect accommodation in LaVO₃ from nonstoichiometric growth conditions caused a reduction of the out-of-plane film lattice parameter, thus enabling the growth window to be identified by a constant and maximum film lattice parameter.²⁴ Therefore, it is not clear which defect accommodation mechanism will dominate and if a maximum or minimum in lattice parameter is expected for stoichiometric La_{1-x}Sr_xVO₃.

High-resolution 2θ - ω scans around the 002 LSAT peak are shown in Fig. 1(a) for stoichiometric LaVO₃, SrVO₃, La_{0.18}Sr_{0.82}VO₃, La_{0.35}Sr_{0.65}VO₃, and La_{0.65}Sr_{0.35}VO₃, as well as La_{0.70}Sr_{0.30}VO₃ for a range of gas inlet pressures P_{VTIP} , which were obtained using Cu-K α_1 radiation. These data allow extraction of the lattice parameter by tracking the film peak position, as well as the film thickness for a subset of films by extracting the periodicity of the Kiessig fringes.

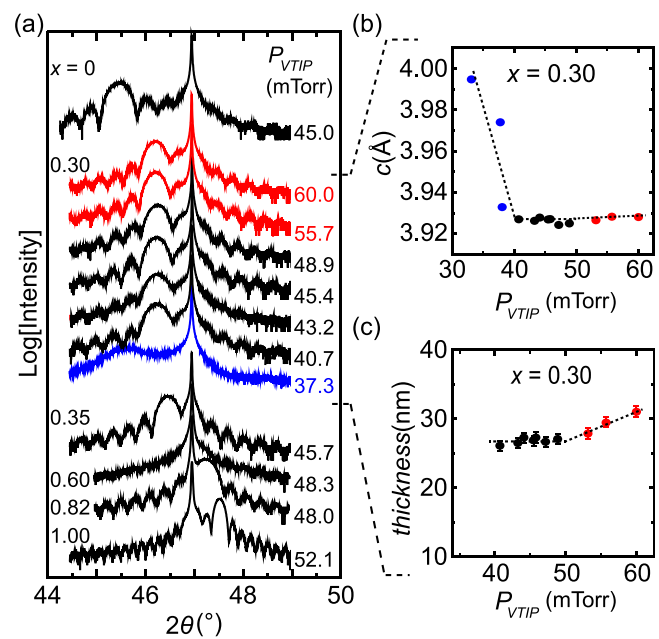


FIG. 1. (a) 2θ - ω scans around the 002 LSAT substrate peak ($2\theta \approx 46.9^\circ$) for La_{1-x}Sr_xVO₃ films with various compositions listed from top to bottom $x = 0.00$ (LaVO₃), $x = 0.30$ (blue: V-deficient, black: stoichiometric, and red: V-rich growth conditions), $x = 0.35$, $x = 0.65$, $x = 0.82$, and $x = 1.00$ (SrVO₃). (b) Out-of-plane lattice parameter versus P_{VTIP} for La_{0.70}Sr_{0.30}VO₃. (c) La_{0.70}Sr_{0.30}VO₃ film thickness extracted from the Kiessig fringes in (a), versus P_{VTIP} .

Figure 1(b) shows the c -axis lattice parameter extracted from the 002 peak from the 2θ - ω scans for $\text{La}_{0.70}\text{Sr}_{0.30}\text{VO}_3$. The behavior for V-deficient and V-rich films is different. For V-deficient films ($P_{VTIP} < 40.0$ mTorr), the lattice parameter sharply increased with increasing deviation from the growth window, whereas for V-rich films ($P_{VTIP} > 49.0$ mTorr), it remained similar to the lattice parameter found within the growth window. This makes XRD analysis unable to determine the A:B cation stoichiometry; however, other measures revealed that the film's properties deteriorated for $\text{La}_{0.70}\text{Sr}_{0.30}\text{VO}_3$ grown with a P_{VTIP} larger than 50.0 mTorr. Figure 1(c) shows the film thickness extracted from the Kiessig fringes³⁴ of the 2θ - ω XRD scans in Fig. 1(a). For V-deficient films, no fringes were observed, which was attributed to the rough film surface morphology, as discussed further below. For all other $\text{La}_{0.70}\text{Sr}_{0.30}\text{VO}_3$ films with $P_{VTIP} > 40$ mTorr, Kiessig fringes were present, indicating atomically flat surfaces. The thickness remained constant at around ~ 26 nm \pm 1.0 nm, irrespective of VTIP supply within the growth window between $P_{VTIP} \approx 40.0$ – 50.0 mTorr. For P_{VTIP} above this range, the film thickness was found to increase by ~ 0.5 nm/mTorr. Together these confirm the existence of an adsorption-controlled growth window. The majority of the error within the growth window likely stems from uncertainty in the net flux as measured *in situ* by QCM, which is significantly small compared to the increase in thickness outside this regime.

Figure 2(a) shows selected RHEED images taken from the $x = 0.30$ series at 900°C along the $\langle 110 \rangle$ (top row) and the $\langle 100 \rangle$ (bottom row). With increasing P_{VTIP} , a qualitative change of the diffraction pattern was observed from V-deficient (34.4 mTorr and 38.0 mTorr) to stoichiometric (42.5 mTorr, 45.4 mTorr, and 45.8 mTorr) growth condition. On the V-deficient side, the main diffraction spots in the RHEED images appeared blurry and of low intensity, providing only a small contrast with respect to the background intensity arising from diffuse scattering. Kikuchi lines were hardly resolved which indicated a more disordered surface. Along the $\langle 100 \rangle$, V-deficient films showed an elongation of

the main diffraction spots, indicating a more pronounced surface roughness. These features were absent in RHEED patterns for films grown within the growth window. The diffraction patterns were very sharp and showed well-defined Kikuchi lines, no elongation of the main diffraction spots into streaks were observed in the diffraction pattern taken along $\langle 100 \rangle$. In contrast to XRD, which could not distinguish V-rich from stoichiometric growth conditions, V-rich films (53.2 mTorr and 60.0 mTorr) showed degradation of the RHEED pattern similar to V-deficient films. For the composition $x = 0$, i.e., SrVO_3 , RHEED revealed superimposed diffraction patterns from intergrowth of additional crystalline phases,²³ and for the growth of SrTiO_3 films surface reconstruction taken at lower-than-growth-temperature have been linked to the film's stoichiometry³⁵—neither diffraction features from secondary phases nor surface reconstructions were observed for $\text{La}_{1-x}\text{Sr}_x\text{VO}_3$ with $x \leq 0.8$. To further corroborate the RHEED analysis, AFM images of the surface morphology for $\text{La}_{0.7}\text{Sr}_{0.3}\text{VO}_3$ grown at these different P_{VTIP} are shown in Fig. 3(b). The surfaces of the stoichiometric films were characterized by clear step-edge features with root means square (RMS) values of ~ 0.5 nm. In contrast, both V-rich and V-deficient films had a more corrugated surface morphology without step edges. In particular, V-deficient films had round features with diameter ~ 100 nm that were roughly ~ 1 nm in height.

We present data showing that the growth window can be mapped entirely with the help of *in situ* RHEED using a single calibration sample by growing repeated layers at different P_{VTIP} . Figure SI 2 (supplementary material) shows RHEED images taken along the $\langle 100 \rangle$ and $\langle 100 \rangle$ for $x = 0, 0.65, 0.82$, and 1.00, at various values of P_{VTIP} . The length of each deposition at a particular P_{VTIP} was long enough, so that surface structure reached equilibrium, which was typically ~ 10 nm, for example, see Fig. SI 3 in the supplementary material. This iterative method is found to not produce surfaces that are as pristine as films grown at a single P_{VTIP} ; however, by analyzing how the diffraction pattern changes one can reliably extract the growth window. As shown in Fig. 3, the end

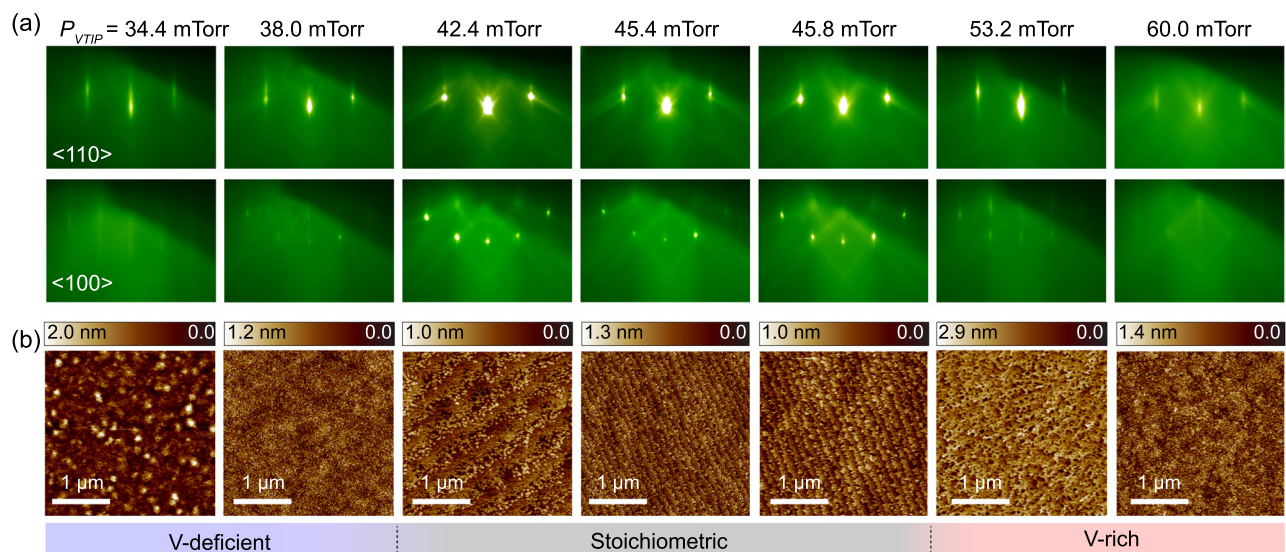


FIG. 2. (a) Reflection-high energy electron-diffraction patterns taken along the $\langle 110 \rangle$ (upper row) and $\langle 100 \rangle$ (bottom row) azimuth of $\text{La}_{0.70}\text{Sr}_{0.30}\text{VO}_3$ films grown at various P_{VTIP} . (b) Corresponding atomic force microscopy images of $\text{La}_{0.70}\text{Sr}_{0.30}\text{VO}_3$ films grown at various P_{VTIP} .

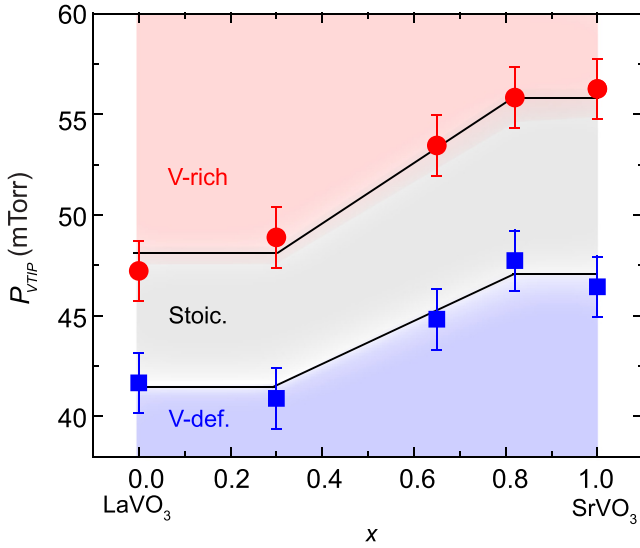


FIG. 3. Growth window evolution for P_{VTIP} versus x extracted from reflection-high energy electron-diffraction patterns shown in Fig. SI2 (supplementary material). Red circles and blue squares indicate the boundaries between the growth window and V-rich and V-deficient growth conditions, respectively. The grey shaded area indicates the range of stoichiometric growth conditions.

members LaVO_3 and SrVO_3 have growth windows from RHEED that nearly coincide with the growth windows previously reported: SrVO_3 $P_{VTIP} \approx 45.0\text{--}52.5$ mTorr²³ and LaVO_3 $P_{VTIP} \approx 39.0\text{--}42.5$ mTorr (Ref. 24 reports samples grown at $2.00 \times 10^{13} \text{ cm}^{-2} \text{ s}^{-1}$, which we just multiplied by $(2.50 \times 10^{13})/(2.00 \times 10^{13})$). The slight difference between the current report and the previous report likely stems from slight differences in the VTIP source material or a technical issue possibly due to drift in the zero point of the capacitance manometer used to measure P_{VTIP} . Nevertheless, applying the same iterative strategy to intermediate members, we see that, within error, the growth window is roughly constant near the end members ($x \leq 0.3$ and $x \geq 0.8$) and becomes linear in between this ($0.3 < x < 0.8$). The error bars that identify the edge of the growth window in Fig. 3 were estimated based on the rough step size used for $P_{VTIP} \sim 1.5$ mTorr and the uncertainty in distinguishing the features of the RHEED patterns at adjacent values of P_{VTIP} , and, therefore, we conservatively took them to be roughly $\sim \pm 1.5$ mTorr.

Finally, with the compositional dependence of the growth window identified, Fig. 4 shows the c -axis lattice parameter versus x for stoichiometric samples (black triangles) as well as selected V-rich (red circles) and V-deficient (blue squares) films. The composition was obtained from RBS measurements taken from calibration samples for $\text{La}_{1-x}\text{Sr}_x\text{VO}_3$ films grown under the same conditions on Al_2O_3 substrates (see supplementary material). The choice of a different substrate was necessary because the LSAT substrate contained both La and Sr, which precluded quantification of La and Sr ratios directly from the films grown on LSAT. Films grown on sapphire were found to be polycrystalline and yielded the composition x to within $\sim 1.5\%$ accuracy. The out-of-plane lattice parameter $c(x)$ did not change linearly with composition, as predicted from Vegard's law³⁶

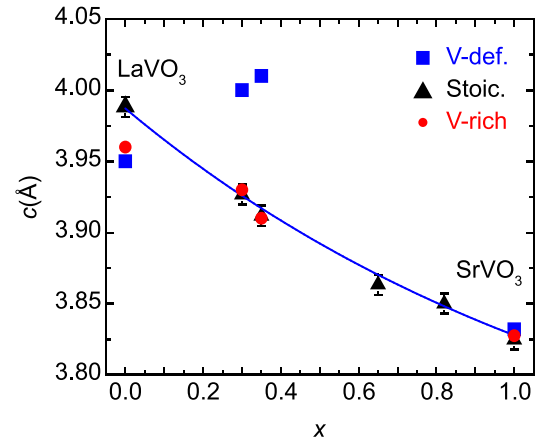


FIG. 4. Out-of-plane lattice parameter versus composition x for V-deficient (blue stars), stoichiometric (black triangles), V-rich (red circles) $\text{La}_{1-x}\text{Sr}_x\text{VO}_3$ films. The solid blue line shows the mismatch corrected out-of-plane film lattice parameter dependence on the film's composition x .

$$a_{LSVO}(x) = a_{LVO}(1-x) + a_{SVO}x, \quad (1)$$

using $a_{SVO} = 3.825$ Å and $a_{LVO} = 3.920$ Å, the lattice parameter for SrVO_3 and LaVO_3 (pseudocubic), respectively, which is in contrast to the linear dependence observed in bulk samples.¹³ The change in the lattice mismatch between film and substrate with composition x needed to be considered here as well because epitaxial mismatch and out-of-plane film lattice parameter c are linked by the Poisson ratio ν in the present case of coherently strained films by

$$c = a_f(1-\nu)/(1+\nu) - 2\nu(1-\nu)a_{LSAT}, \quad (2)$$

where ν is the Poisson ratio of the material, a_{LSAT} and a_f the substrate and unstrained film lattice parameter. Assuming that the Poisson ratio $\nu(x)$ of the quaternary compound $\text{La}_{1-x}\text{Sr}_x\text{VO}_3$ can be linearly interpolated from the Poisson ratio of the end member of the solid solution

$$\nu(x) = \nu_{LVO}(1-x) + \nu_{SVO}(x), \quad (3)$$

where ν_{LVO} and ν_{SVO} are the Poisson ratios for LaVO_3 and SrVO_3 , respectively, we obtain a non-linear relationship for the composition dependence of the out-of-plane film lattice parameter $c(x)$ by substituting Eqs. (1) and (3) into Eq. (2). Using the Poisson ratios ν_{LVO} and ν_{SVO} as fitting parameters, an epitaxial mismatch corrected dependence of the out-of-plane film lattice parameter was obtained for stoichiometric $\text{La}_{1-x}\text{Sr}_x\text{VO}_3$ films shown as blue solid line in Fig. 4, which yielded $\nu_{LVO} = 0.398$ and $\nu_{SVO} = 0.214$;^{23,29,37-39} the Poisson ratio for SrVO_3 matched previously reported values,^{23,29} while the value of 0.398 for LaVO_3 was within physically reasonable values. The out-of-plane film lattice parameter therefore provides a means to obtain the composition x of stoichiometric $\text{La}_{1-x}\text{Sr}_x\text{VO}_3$ films without the need for RBS measurements provided the growth window can be confirmed by RHEED.

To conclude, we have optimized the growth condition for the quaternary compound $\text{La}_{1-x}\text{Sr}_x\text{VO}_3$ by hMBE as a function of composition x using a combination of XRD, RHEED, AFM, and RBS. Unlike the ternary end members of the solid solution, where a growth window was identified

from the changes in the film lattice parameter as a function of P_{VTIP} pressure, a significant change in film lattice parameter of $\text{La}_{1-x}\text{Sr}_x\text{VO}_3$ with $x = 0.30$ was only found for V-deficient, but not for V-rich growth conditions. The boundary between stoichiometric and V-rich side conditions was thus identified by an increase in film thickness, degradation of the RHEED pattern, and changes in the surface morphology observed in AFM. The growth window changes were mapped as a function of A-site composition x using RHEED. A composition series with stoichiometric $\text{La}_{1-x}\text{Sr}_x\text{VO}_3$ was grown and La/Sr ratio was extracted using a lattice mismatch corrected expression for the out-of-plane film lattice parameter, which was found in good comparison with RBS measurements. The simplified scheme to utilize RHEED for the identification of a growth window combined with the extraction of A site composition from XRD provides an effective and straight forward strategy to map out stoichiometric growth conditions using a single calibration sample and determine the film's actual composition, paving the way to optimize technologically relevant quaternary oxide systems, such as high- T_C superconductors, piezo- and ferroelectric materials and charge ordered systems exhibiting colossal magnetotransport phenomena.

See [supplementary material](#) for RBS data and methods and extended RHEED analysis.

M.B. and R.E.H. acknowledge the Department of Energy (Grant No. DE-SC0012375) for the growth, XRD, AFM measurements, and preparation of the manuscript. L.Z., J.M.L., and H.T.Z. assisted in the growth and acknowledge support from the National Science Foundation through the Penn State MRSEC Program DMR-1420620 (J.M.L., H.T.Z., and R.E.H.) as well as NSF Career Grant No. DMR-1352502 (L.Z. and R.E.H.). L.R.D. and L.W.M. acknowledge support from the U.S. Department of Energy under Grant No. DE-SC0012375 for RBS measurements and analysis.

- ¹M. Imada, A. Fujimori, and Y. Tokura, *Rev. Mod. Phys.* **70**, 1039 (1998).
- ²P. A. Lee and X.-G. Wen, *Rev. Mod. Phys.* **78**, 17 (2006).
- ³S.-Y. Xu, Y. Xia, L. A. Wray, S. Jia, F. Meier, J. H. Dil, J. Osterwalder, B. Slomski, A. Bansil, H. Lin, R. J. Cava, and M. Z. Hasan, *Science* **332**, 560 (2011).
- ⁴T. Sato, K. Segawa, K. Kosaka, S. Souma, K. Nakayama, K. Eto, T. Minami, Y. Ando, and T. Takahashi, *Nat. Phys.* **7**, 840 (2011).
- ⁵M. Brahlek, N. Bansal, N. Koirala, S.-Y. Xu, M. Neupane, C. Liu, M. Z. Hasan, and S. Oh, *Phys. Rev. Lett.* **109**, 186403 (2012).
- ⁶Y. Tokura and Y. Tomioka, *J. Magn. Magn. Mater.* **200**, 1 (1999).
- ⁷M. Jaros, *Rep. Prog. Phys.* **48**, 1091 (1985).

- ⁸B. Jaffe, W. R. Cook, Jr., and H. Jaffe, *Piezoelectric Ceramics* (Academic Press, London/New York, 1971).
- ⁹J. G. Bednorz and K. A. Muller, *Z. Phys. B: Condens. Matter* **64**, 189 (1986).
- ¹⁰G. H. Jonker and J. H. Van Santen, *Physica* **16**, 337 (1950).
- ¹¹J. Volger, *Physica* **20**, 49 (1954).
- ¹²J. H. Van Santen and G. H. Jonker, *Physica* **16**, 599 (1950).
- ¹³A. V. Mahajan, D. C. Johnston, D. R. Torgeson, and F. Borsa, *Phys. Rev. B* **46**, 10973 (1992).
- ¹⁴F. Inaba, T. Arima, T. Ishikawa, T. Katsufuji, and Y. Tokura, *Phys. Rev. B* **52**, R2221 (1995).
- ¹⁵Y. Tokura, *J. Phys. Chem. Solids* **53**, 1619 (1992).
- ¹⁶K. Byczuk, W. Hofstetter, and D. Vollhardt, *Phys. Rev. Lett.* **94**, 056404 (2005).
- ¹⁷T. Ohnishi, K. Shibuya, T. Yamamoto, and M. Lippmaa, *J. Appl. Phys.* **103**, 103703 (2008).
- ¹⁸R. Engel-Herbert, *Molecular Beam Epitaxy From Research to Mass Production* (Elsevier Science, 2013), Chap. 17.
- ¹⁹B. Jalan, P. Moetakef, and S. Stemmer, *Appl. Phys. Lett.* **95**, 032906 (2009).
- ²⁰Y. Matsubara, K. S. Takahashi, Y. Tokura, and M. Kawasaki, *Appl. Phys. Express* **7**, 125502 (2014).
- ²¹P. Moetakef, D. G. Ouellette, J. Y. Zhang, T. A. Cain, S. J. Allen, and S. Stemmer, *J. Cryst. Growth* **355**, 166 (2012).
- ²²P. Xu, D. Phelan, J. Seok Jeong, K. Andre Mkhoyan, and B. Jalan, *Appl. Phys. Lett.* **104**, 082109 (2014).
- ²³M. Brahlek, L. Zhang, C. Eaton, H.-T. Zhang, and R. Engel-Herbert, *Appl. Phys. Lett.* **107**, 143108 (2015).
- ²⁴H.-T. Zhang, L. R. Dedon, L. W. Martin, and R. Engel-Herbert, *Appl. Phys. Lett.* **106**, 233102 (2015).
- ²⁵A. Prakash, J. Dewey, H. Yun, J. S. Jeong, K. A. Mkhoyan, and B. Jalan, *J. Vac. Sci. Technol. A* **33**, 060608 (2015).
- ²⁶J. Son, P. Moetakef, B. Jalan, O. Bierwagen, N. J. Wright, R. Engel-Herbert, and S. Stemmer, *Nat. Mater.* **9**, 482 (2010).
- ²⁷B. Jalan, S. J. Allen, G. E. Beltz, P. Moetakef, and S. Stemmer, *Appl. Phys. Lett.* **98**, 132102 (2011).
- ²⁸Y. Matsubara, K. S. Takahashi, M. S. Bahramy, Y. Kozuka, D. Maryenko, J. Falson, A. Tsukazaki, Y. Tokura, and M. Kawasaki, *Nat. Commun.* **7**, 11631 (2016).
- ²⁹J. A. Moyer, C. Eaton, and R. Engel-Herbert, *Adv. Mater.* **25**, 3578 (2013).
- ³⁰J. Y. Tsao, *Materials Fundamentals of Molecular Beam Epitaxy* (Academic Press, Inc., San Diego, 1993).
- ³¹E. Mikheev, A. P. Kajdos, A. J. Hauser, and S. Stemmer, *Appl. Phys. Lett.* **101**, 252906 (2012).
- ³²J. B. Goodenough, *Rep. Prog. Phys.* **67**, 1915 (2004).
- ³³C. Eaton, J. A. Moyer, H. M. Alipour, E. D. Grimley, M. Brahlek, J. M. LeBeau, and R. Engel-Herbert, *J. Vac. Sci. Technol. A* **33**, 061504 (2015).
- ³⁴J. M. LeBeau, R. Engel-Herbert, B. Jalan, J. Cagnon, P. Moetakef, S. Stemmer, and G. B. Stephenson, *Appl. Phys. Lett.* **95**, 142905 (2009).
- ³⁵A. P. Kajdos and S. Stemmer, *Appl. Phys. Lett.* **105**, 191901 (2014).
- ³⁶A. R. Denton and N. W. Ashcroft, *Phys. Rev. A* **43**, 3161 (1991).
- ³⁷I. R. Shein, V. L. Kozhevnikov, and A. L. Ivanovskii, *Solid State Sci.* **10**, 217 (2008).
- ³⁸T. Maekawa, K. Kurosaki, and S. Yamanaka, *J. Alloys Compd.* **426**, 46 (2006).
- ³⁹A. Parveen and N. K. Gaur, *Phys. B: Condens. Matter* **407**, 500 (2012).